Chemical Engineering Journal 496 (2024) 154337

Contents lists available at ScienceDirect

Chemical Engineering Journal

journal homepage: www.elsevier.com/locate/cej

Plasma-catalytic direct oxidation of methane to methanol over Cu-MOR: Revealing the zeolite-confined Cu^{2+} active sites

Huan Lv [a,b,1], Shengyan Meng [a,1], Zhaolun Cui [c,1], Shangkun Li [d], Dongxing Li [d], Xiaoxia Gao [e], Hongchen Guo [a], Annemie Bogaerts [d], Yanhui Yi [a,*]

[a] State Key Laboratory of Fine Chemicals, Frontier Science Center for Smart Materials, School of Chemical Engineering, Dalian University of Technology, Dalian 116024, PR China
[b] Baotou Electrical Industrial Vocational School, Baotou 014000, PR China
[c] School of Electric Power Engineering, South China University of Technology, Guangzhou 510630, PR China
[d] Research Group PLASMANT, Department of Chemistry, University of Antwerp, Universiteitsplein 1, BE-2610 Wilrijk-Antwerp, Belgium
[e] Instrumental Analysis Center, Dalian University of Technology, Dalian 116024, PR China

ARTICLE INFO

Keywords:
Methane conversion
Direct oxidation
Methanol production
Plasma catalysis
Copper-mordenite catalysts

ABSTRACT

Efficient methane conversion to methanol remains a significant challenge in chemical industry. This study investigates the direct oxidation of methane to methanol under mild conditions, employing a synergy of non-thermal plasma and Cu-MOR (Copper-Mordenite) catalysts. Catalytic tests demonstrate that the Cu-MOR IE-3 catalyst (i.e., prepared by three cycles of ion exchange) exhibits superior catalytic performance (with 51 % methanol selectivity and 7.9 % methane conversion). Conversely, the Cu-MOR catalysts prepared via wetness impregnation tend to over-oxidize CH_4 to CO and CO_2. Through systematic catalyst characterizations (XRD, TPR, UV–Vis, HRTEM, XPS), we elucidate that ion exchange mainly leads to the formation of zeolite-confined Cu^{2+} species, while wetness impregnation predominantly results in CuO particles. Based on the catalytic performance, catalyst characterizations and *in-situ* FTIR spectra, we conclude that zeolite-confined Cu^{2+} species serve as the active sites for plasma-catalytic direct oxidation of methane to methanol.

1. Introduction

The industrial conversion of methane (CH_4) to methanol (CH_3OH) typically follows an indirect route, involving the initial step of CH_4 steam reforming to generate syngas (CO and H_2) at elevated temperature (above 800 °C). Subsequently, the synthesis of CH_3OH takes place at high pressure (ca. 100 atm) using a Cu-Zn-Al catalyst. Although widely applied on a large scale, this commercial method is unsuitable for small-scale production due to its demanding reaction conditions, intricate operational processes, energy-intensive requirements and high equipment costs [1]. Consequently, there is a growing interest in the direct oxidation of methane to methanol (DOMtM) under mild conditions, offering significant potential for implementation at distributed and small-scale plants [2]. For over a century, researchers have explored DOMtM through both homogeneous and heterogeneous catalysis. Homogeneous catalysis typically involves the use of fuming sulfuric acid [3] or trifluoroacetic acid [4] as reaction solvents. Complex catalysts featuring Pt, Pd, Au or Hg noble metals as active centers have been employed. In the realm of heterogeneous catalysis, various catalytic materials, including metals [5] and metal oxides [6] have been intensely investigated.

Recently, inspired by the binuclear iron and copper active sites observed in natural methane monooxygenase (MMO), researchers have explored iron- and copper-based zeolite catalysts for DOMtM with high selectivity [7]. Iron-based zeolites exhibit proficient N_2O decomposition ($N_2O + (Fe^{2+})_\alpha \rightarrow (Fe^{3+}\text{-}O^-)_\alpha + N_2$) at temperatures below 300 °C, with the α-O species identified as the active component for DOMtM [8]. Copper-based zeolites show notable catalytic efficacy in DOMtM, especially when O_2 or H_2O is employed as oxidants, positioning Cu-MOR as a highly promising catalytic material for DOMtM [9]. To overcome the high energy barrier (E_a) of CH_4 oxidation and to inhibit excessive oxidation of CH_3OH, a multi-step chemical looping approach has been proposed. This method involves catalyst pre-activation of the catalyst with O_2 at high temperatures, followed by a low-temperature reaction

* Corresponding author.
E-mail address: yiyanhui@dlut.edu.cn (Y. Yi).
[1] H.L., S.M. and Z.C. contributed equally to this paper.

https://doi.org/10.1016/j.cej.2024.154337
Received 6 April 2024; Received in revised form 16 July 2024; Accepted 26 July 2024

with CH_4 to generate adsorbed CH_3OH species. Subsequently, extraction through either solvent or steam leads to the production of CH_3OH. The primary objective of this approach is to safeguard the CH_3OH formed on the catalyst surface from excessive oxidation, thereby achieving a superior CH_3OH selectivity exceeding 90 %. However, the intricate multi-step process involves frequent switches in feeding gases and adjustments in temperature, introduces discontinuities in CH_3OH production, diminishes overall reaction efficiency, and entails substantial energy consumption.

Non-thermal plasma (NTP) stands out as a powerful method for activating and converting CH_4 to CH_3OH. Energetic electrons within the NTP effectively activate CH_4 and O_2 molecules, generating reactive radical species (CH_x and O species) [10,11]. Additionally, the low gas temperature in NTP plays a crucial thermodynamic role in CH_3OH production, as excessively high temperatures can lead to CH_3OH decomposition or its reforming with water vapor, producing CO and CO_2. A dielectric barrier discharge (DBD) is one of the most common methods to produce NTP and is widely employed in plasma-assisted DOMtM. Nozaki demonstrated the conversion of CH_4 into oxygenates in a microplasma reactor with a single-pass yield of 5–20 % and a selectivity of 70–30 % [12]. Furthermore, when employing a Cu/ZnO/Al_2O_3 (CZA) catalyst for DOMtM, oxidized Cu species exhibited higher CH_3OH selectivity compared to copper metal (Cu^0) species, suggesting that Cu^+ or Cu^{2+} may serve as active components in plasma-assisted DOMtM [13]. Subsequently, Chawdhury et al. found that a CuO/γ-Al_2O_3 catalyst enhanced the CH_3OH selectivity, with high Cu loading facilitating formaldehyde (HCHO) generation [14]. Recently, Li et al. reported a strategy to overcome the trade-off relationship between CH_4 conversion and CH_3OH selectivity through co-feeding H_2O vapor with CH_4 and O_2 over a Pt_2/BN-na catalyst [9].

Zeolite-supported Cu catalysts have been studied by other researchers for DOMtM under NTP conditions. Song's group used Cu-MOR zeolite and NTP to produce CH_3OH from CH_4 and H_2O at 120 °C without CO_2 formation, achieving an energy efficiency of 68.8 mmol/kJ and a CH_3OH selectivity of 86 % [15]. In summary, Cu-based zeolite catalysts exhibit notable CH_3OH selectivity in thermal catalytic DOMtM, while NTP facilitates DOMtM with impressive CH_4 conversion at low temperatures. Consequently, the synergistic utilization of NTP and Cu-based zeolite catalysts emerges as a promising strategy for DOMtM.

This study systematically compares the performance of Cu-MOR catalysts prepared using both wetness impregnation and ion exchange methods in plasma-catalytic DOMtM. We systematically investigate the catalytic performance and the nature of the active sites formed by each preparation method, utilizing Bolsig + calculations to study the catalyst and reaction processes. Furthermore, *in-situ* FTIR spectroscopy is employed to elucidate the differences in intermediates on various active sites, providing deeper insights into the reaction mechanism. These comprehensive studies not only demonstrate the superior performance of ion-exchanged Cu-MOR catalysts but also reveal the critical role of zeolite-confined Cu^{2+} species in enhancing the selectivity and conversion of CH_4 to CH_3OH under NTP conditions.

1.1. Catalyst preparation

The Cu-based catalysts were synthesized using both ion exchange and wetness impregnation methods, as illustrated in Supporting Information (Scheme S1). Commercial MOR zeolite (purchased from Nankai University Catalyst Co., Ltd.) was calcined in a muffle furnace at 400 °C for 5 h. $Cu(CH_3COO)_2{\cdot}H_2O$ and $Cu(NO_3)_2{\cdot}3H_2O$ (provided by Shanghai Aladdin Biotechnology Co.) were used as the copper sources for ion exchange and wetness impregnation, respectively. For the ion exchange method, 10 g MOR zeolite was added to 28 ml $Cu(CH_3COO)_2{\cdot}H_2O$ solution (0.4mol$_{Cu}$/l), stirred, and placed in a 90 °C water bath for 2 h. Then, the samples were filtered, washed and dried overnight at 100 °C. Subsequently, the dried samples were calcined in a muffle furnace at 540 °C for 5 h, yielding the ion-exchanged Cu-MOR, designated as Cu-MOR IE-1. To further enhance the Cu loading, various cycles of ion exchange (2, 3, 4, and 5) were used to synthesize Cu-MOR catalysts based on the Cu-MOR IE-1 sample. These samples, prepared through multiple ion exchanges, are denoted as Cu-MOR IE-2, Cu-MOR IE-3, Cu-MOR IE-4 and Cu-MOR IE-5. The wetness impregnation method involved dissolving $Cu(NO_3)_2{\cdot}3H_2O$ in deionized water, adding MOR zeolite to the solution with calculated loading, and stirring intensively. After aging at room temperature for 12 h, the samples were dried at 120 °C overnight and calcined in a muffle furnace at 540 °C for 5 h. Finally, the obtained samples are denoted as X wt.% Cu-MOR (X=2, 5, 10, 15, and 20) based on different Cu loadings. Detailed information on the process can be found in the Supporting Information.

1.2. Catalytic tests

The experimental setup is shown in Scheme S2. Calibrated mass flow controllers were used to control the flow rate of CH_4 and O_2 (both 99.999 % purity), which were mixed well before flowing into the DBD reactor. The DBD reactor, featuring two layers of quartz glass, comprised an inner tube with a 10 mm outer diameter filled with 1.25 g catalyst granules (20–40 mesh). The outer tube had a 30 mm outer diameter, and there was circulated water between both tubes, functioning both as a temperature control for the discharge area and as the grounding electrode. A 2 mm stainless steel rod placed inside the inner tube, was used as the high voltage electrode.

The effective length of the discharge area was fixed at 50 mm. Throughout plasma-assisted DOMtM, the discharge frequency was set at 9.2 kHz. The discharge voltage, current and input power were monitored using a digital oscilloscope (DPO 3012, Tektronix, USA). The gas flow rates before and after reaction were measured by a mass flow controller to account for volume compression or expansion due to the chemical reaction, when determining the CH_4 conversion and product yield/selectivity. Gas products were analyzed using a gas chromatograph (GC-7900, Tianmei, China) with a thermal conductivity detector (TDX-01 column) and a flame ionization detector (alumina-filled column). Liquid products were condensed in a cold trap (a mixture of isopropanol and liquid nitrogen) and subsequently analyzed using a gas chromatograph (GC-2014C, Shimadzu, Japan), GC–MS (5975C, Agilent, USA), and ^{1}H NMR (AVANCE III 500, Bruker, Switzerland). Further details on the qualitative and quantitative analysis of products in CH_4/O_2 NTP are provided in SI, including the formulas of the standard calibrated concentration curves (presented in Table S1). Each catalyst underwent three tests to establish experimental error bars. The quantitative analysis of the product is shown in Fig. S1.

To evaluate the reaction performance of the catalysts, the selectivity of reaction products and the CH_4 conversion were calculated using the following equations. Carbon-based selectivity is defined here, excluding H_2O and H_2 from these equations.

The CH_4 conversion was calculated by:

$$X_{CH_4}\ (\%) = \frac{\text{moles of } CH_4 \text{ converted}}{\text{moles of initial } CH_4} \times 100\ \% \quad (1)$$

In the gaseous products, only trace amounts of hydrocarbons (selectivity less than 0.1 %) were detected. Therefore, the gaseous products are considered to consist solely of CO and CO_2, with selectivity calculated as follows:

$$S_{CO}\ (\%) = \frac{\text{moles of CO produced}}{\text{moles of } CH_4 \text{ converted}} \times 100\ \% \quad (2)$$

$$S_{CO_2}\ (\%) = \frac{\text{moles of } CO_2 \text{ produced}}{\text{moles of } CH_4 \text{ converted}} \times 100\ \% \quad (3)$$

The carbon deposition of the catalyst after the reaction was evaluated to be negligible by thermogravimetric analysis (TGA) and mass spectrum (MS) (Fig. S2), and the selectivity of the liquid products was calculated as follows:

Total selectivity of liquid products (\%) = 100 \% -) = 100{%− (S_{CO} +S_{CO_2}) (4)

The selectivity of every single oxygenates, $C_xH_yO_z$, can be calculated as:

$$S_{C_xH_yO_z}(\%)) = \frac{X \times N_{C_xH_yO_z}}{\sum X_i N_i} \times \text{total selectivity of liquid products} \quad (5)$$

where $N_{C_xH_yO_z}$ represents the number of moles of various oxygenates in the liquid fraction.

Finally, we defined the energy consumption for CH_3OH formation (kJ/mmol) as:

$$\text{Energy consumption (kJ/mmol)} = \frac{\text{discharge power (J/s)}}{\text{rate of } CH_3OH \text{ produced (mol/s)}} \times 10^{-6} \quad (6)$$

1.3. Catalyst characterization

The crystal structure of the catalyst was determined using an X-ray diffractometer (Rigaku, D-max 2400) with CuKα radiation. The measurement was operated in the range of 10-80° with a scanning rate of 5°/min at 50 mA and 240 kV. The specific surface area, pore volume, and pore size of the catalysts were analyzed by N_2 physisorption. The samples (0.15 g) were evacuated for 4–6 h at 350 °C for pretreatment to remove water and other impurities in the pores. N_2 adsorption–desorption measurements were carried out at −196 °C. The Brunauer-Emmett-Teller method was used to calculate the total specific surface area of the samples, and the t-plot method was used to calculate the specific surface area and the pore volume. The total pore volume was calculated as the N_2 adsorption at a relative pressure of $p/p_0 = 0.99$. The elementary composition of the catalysts was determined by X-ray fluorescence spectroscopy (XRF) using a X-ray fluorescence spectrometer (SRS 3400, Bruker, Germany). The reduction properties of the catalysts were measured on a ChemBET Pulsar (Quanta chrome) chemical adsorption instrument. The samples (0.15 g) were purged for 1 h at 550 °C under He atmosphere. After cooling to room temperature, the samples were heated to 700 °C at a rate of 10 °C/min in an Ar-H_2 atmosphere (120 mL/min, 10 % H_2), and a TCD was used to detect the hydrogen consumption. Characterization of Cu species on the catalyst surface was performed by a UV–Visible (UV–Vis) spectrophotometer (UV-550, Agilent, USA) with integrating sphere attachment (built-in dra2500). The diffuse reflectance spectra were collected in the range of 190–900 nm using $BaSO_4$ white plate as a reference. The morphology of the catalysts was observed by electron microscopy. The scanning electron microscope (SEM) model was Hitachi S-4800 field emission electron microscope with acceleration voltage of 2–30 kV. The size and dispersion of the loaded metals in the catalysts were analyzed using high-resolution transmission electron microscopy (HRTEM) with an instrument model Tecnai G2 F30 S-Twin (300 kV). X-ray photoelectron spectroscopy (XPS) was conducted by Thermo Fisher ESCALAB XI+with an Al Kα X-ray source. In the *in-situ* Fourier Transform Infrared (FTIR) spectroscopy setup, we utilized a Thermo Nicolet iS10 spectrometer equipped with a deuterated triglycine sulfate (DTGS) detector. The scanning range was 400 to 4000 cm^{-1}, with each scan repeated 64 times and a resolution set at 4.0 cm^{-1}. A 0.05 g catalyst sample was pressed into a self-supporting wafer with a diameter of 8 mm and placed in an infrared cell fitted with CaF_2 windows (Fig. S3). Plasma was generated between the high-voltage electrode and the ground electrode using external circulating cooling water, with a discharge gap of 8 mm. Before collecting the background, the sample was pretreated in a CH_4/O_2 mixture with a molar ratio of 4:1 for 15 min, followed by plasma ignition to collect the signals. CO Diffuse Reflectance Infrared Fourier Transform Spectroscopy (CO-DRIFTS) was conducted using a Nicolet 6700 Fourier transform infrared spectrometer. Each spectrum was obtained by averaging 64 scans with a resolution of 4 cm^{-1} over the range of 4000–400 cm^{-1}. The DRIFTS cell (Harrick, HVC-DRP) equipped with ZnSe windows served as the reaction chamber. Prior to each DRIFTS experiment, catalysts were purged with N_2 at 200 °C for 2 h, maintaining a flow rate of 40 mL/min. Subsequently, the catalyst was exposed to a CO-Ar flow (2 % CO, 10 mL/min) at 25 °C for 30 min for data collection.

1.4. Plasma diagnostics

The active species in the CH_4/O_2 NTP were detected by *in-situ* optical emission spectroscopy (OES). The instrument model used was a SP 2758 spectrometer from Princeton Instruments, USA, detection range: 200–1100 nm, slit width: 50 μm, exposure time 1 s. During the measurements, the optical fiber probe was positioned close to the outer wall of the reactor, perpendicular to the discharge zone, to capture the signals directly from the plasma while minimizing interference from surface discharges and ambient air. A digital oscilloscope was used to detect the voltage and current signal during the discharge process, and used as a reference to calculate the plasma power, which is important to calculate the energy consumption and energy efficiency of the system. The instrument model used is Tektronix DPO 3012, the high voltage probe model is Tektronix P6015A, and the current probe model is Pearson 6585. Using an infrared thermal imaging camera, the temperature of the plasma region was measured, as detailed in Section 9 of the Supporting Information. The computational details for calculating the MEE and EEDF are provided in the Supporting Information (Section 10).

2. Results and discussion

2.1. Catalytic performance

Fig. 1a and b illustrate the comparative catalytic performance of Cu-MOR catalysts prepared via ion exchange and wetness impregnation methods in DOMtM. In Fig. 1a, the CH_4 conversion and CH_3OH selectivity of Cu-MOR catalysts demonstrate a volcano trend with increasing ion exchange cycles. Cu-MOR IE-3 exhibits the optimal catalytic performance, achieving 7.9 % CH_4 conversion, 51 % CH_3OH selectivity, and 72 % total selectivity for liquid oxygenates. As shown in Fig. 1b, the Cu-MOR catalysts prepared through wetness impregnation reveal a gradual increase in CH_4 conversion but a gradual decrease in CH_3OH selectivity with increasing Cu loading, ranging from 2 wt% to 20 wt%. The 2 wt% Cu-MOR catalyst displays 6.4 % CH_4 conversion with 48 % CH_3OH selectivity, slightly lower than the results of the Cu-MOR IE-3 catalyst. Conversely, the 20 wt% Cu-MOR catalyst exhibits 77 % CO_2 selectivity, 17 % total liquid oxygenates selectivity, and only 12 % CH_3OH selectivity. The selectivity of other liquid products is shown in Table S2. These experimental results suggest that the Cu-MOR IE-3 catalyst demonstrates superior performance in plasma-catalytic DOMtM.

Fig. 1c presents a comparative analysis of the DOMtM reaction outcomes for different modes. In the case of using only a catalyst (Cu-MOR IE-3), the CH_4 conversion is zero, indicating that CH_4 cannot be converted at 20 °C and atmospheric pressure without plasma assistance. For “plasma only” conditions, a CH_4 conversion of 3.6 % is achieved with 32 % CH_3OH selectivity. Introducing MOR as the packing material for plasma results in a CH_4 conversion and CH_3OH selectivity of 4.0 % and 34.5 %, respectively, hence similar to the plasma-only results. This suggests that pure MOR zeolite lacks active sites for DOMtM. However, substituting MOR with the Cu-MOR IE-3 catalyst significantly enhances the reaction performance, indicating a synergistic effect between plasma and the copper active sites on Cu-MOR IE-3 catalyst for DOMtM. This enhancement leads to improved CH_4 conversion (7.9 %) and CH_3OH selectivity (51 %).

Fig. 1d depicts the comparison of these modes in terms of energy consumption, which also serves as a crucial indicator for plasma-

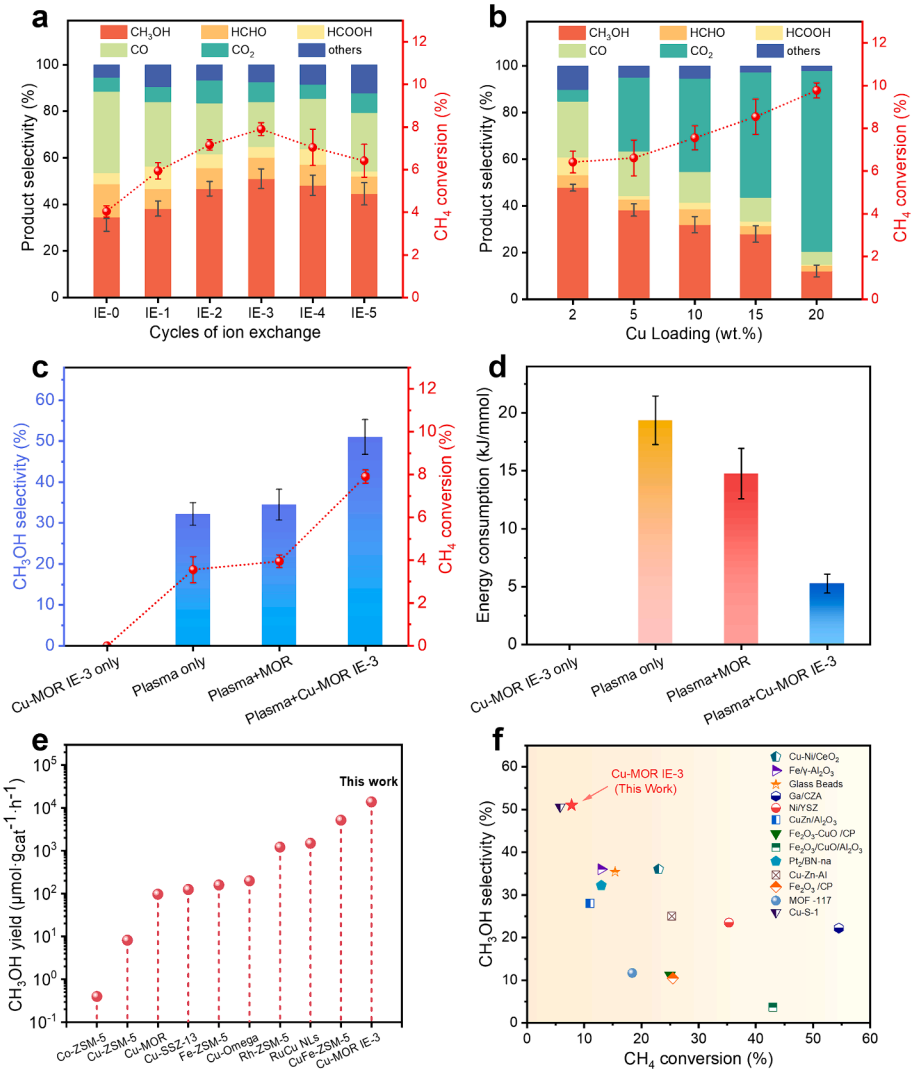

Fig. 1. Experimental results of DOMtM. (a) Cu-MOR catalysts prepared by ion exchange, (b) Cu-MOR catalysts prepared by wetness impregnation, (c) Comparison of "only Cu-MOR IE-3 catalyst", "plasma only", "plasma + MOR", and "plasma + Cu-MOR IE-3" for CH_3OH selectivity and CH_4 conversion, and (d) for energy consumption of CH_3OH production, (e) Comparison of this work with literature results for CH_3OH yield (or productivity) by stoichiometric chemical looping using different catalysts, (f) Comparison of this work with literature results of CH_3OH selectivity and CH_4 conversion using different catalysts. Reaction conditions: 160 ml/min CH_4, 40 ml/min O_2, 20 °C circulating water, 1.25 g catalyst, 25 W input power and 1.178 s residence time.

catalytic DOMtM. The energy consumption for CH_3OH synthesis in the "plasma + Cu-MOR IE-3" system is 5.2 kJ/mmol, which is much lower than that of "plasma only" (19.3 kJ/mmol) and "plasma + MOR" (14.7 kJ/mmol). The energy consumption results of using different catalysts in the literature were compared in Fig. S4 and Table S3.

Comparison with literature results is presented in Fig. 1e and 1f. Fig. 1e reveals that the CH_3OH productivity (13877 $\mu mol \cdot gcat^{-1} \cdot h^{-1}$) surpasses the best outcomes achieved through stoichiometric chemical looping by an order of magnitude [16]. Additionally, as depicted in Fig. 1f, the CH_3OH selectivity exceeds literature results from plasma catalysis using various catalysts, albeit at a lower CH_4 conversion. Notably, a high CH_4 conversion and high CH_3OH selectivity is challenging to achieve simultaneously, as observed by many researchers [16,17]. Consequently, the CH_3OH yield will always be limited in the DOMtM process.

In summary of the above experimental findings, the catalytic performance of Cu-MOR catalysts prepared via ion exchange generally surpasses that of the catalysts prepared through wetness impregnation. Notably, the Cu-MOR IE-3 catalyst, synthesized via ion exchange, exhibits the highest catalytic performance in plasma-assisted DOMtM. Furthermore, the Cu-MOR catalyst prepared through wetness impregnation, particularly with low loading (2 wt%), also demonstrates reasonable catalytic performance, although slightly lower than that of Cu-MOR IE-3. It is noteworthy that altering the preparation method (ion exchange vs wetness impregnation), increasing the number of ion exchange cycles, and enhancing the loading of wetness impregnation can lead to the formation of different metal species on zeolites. Consequently, the diverse catalytic performance of the catalysts is closely linked to the variation in copper species present on the Cu-MOR catalysts.

2.2. Characterization of Cu-MOR catalysts

In order to identify the copper species present on the Cu-MOR catalysts, we employed a comprehensive array of techniques for sample characterization, including XRF, XRD, H_2-TPR, UV–Vis, XPS, and HRTEM. The elemental composition of Si, Al, and Cu in the Cu-MOR catalysts was quantified using XRF, and the results are shown in Table S4. The Si/Al ratio of the purchased commercial MOR zeolite is approximately 17, and the Si/Al ratio of the Cu-MOR samples oscillates around this value. The Cu/Al ratio of the Cu-MOR samples increases slowly with increasing number of ion exchanges. Conversely, for the

samples prepared via wetness impregnation, the Cu/Al ratio significantly rises with increasing Cu loading. Correlating these findings with the catalytic performance depicted in Fig. 1, a volcano-type trend emerges, highlighting an optimal Cu loading range of ca. 2–4 wt%. The effects of Cu loading on the specific surface area and pore volume of MOR zeolite was investigated using N_2-physisorption, and the results are also shown in Table S4. The specific surface area and pore volume of the Cu-MOR samples exhibit a slight decrease with increasing number of ion exchange cycles, primarily attributed to the higher presence of Cu species. Conversely, for the Cu-MOR samples prepared by wetness impregnation, a substantial decrease in specific surface area and pore volume is observed with increasing Cu loading. This drop may be attributed to the presence of CuO particles on the MOR support. The adsorption and desorption curves of MOR and Cu-MOR samples are depicted in Fig. S5, illustrating that the MOR support is a typical microporous material with a microporous volume of 0.18 cm^3g^{-1}. The grain size and morphology of the MOR support and Cu-MOR IE-3 catalyst were characterized by SEM, as shown in Fig. S6. It is evident that the grain size of the MOR zeolite is approximately 250 nm, and both the grain size and morphology of the MOR zeolite remain unchanged after Cu loading.

Fig. 2a and 2b present the XRD patterns of the MOR support and Cu-MOR catalysts, synthesized through ion exchange and wetness impregnation methods, respectively. All samples exhibit well-defined diffraction peaks corresponding to MOR zeolite, indicating the preservation of the MOR lattice structure during the preparation process. In Fig. 2a, the XRD patterns of Cu-MOR catalysts prepared by ion exchange reveal an absence of characteristic diffraction peaks associated with CuO, Cu_2O, or Cu, suggesting that copper species are highly dispersed on MOR [18]. In contrast, in Fig. 2b, the XRD patterns of Cu-MOR catalysts prepared by wetness impregnation display distinct diffraction peaks of CuO (1 1 1) and CuO (−1 1 1). The intensities of these peaks increase proportionally with higher Cu loadings, indicating the formation of larger CuO particles at elevated Cu loadings.

In Fig. 2d, the Cu-MOR samples prepared by wetness impregnation exhibit a distinct reduction peak in the temperature range of 200–400 °C, indicating a one-step reduction of bulk CuO particles ($CuO+H_2 \rightarrow Cu + H_2O$) [19,20]. This observation aligns with the predominant presence

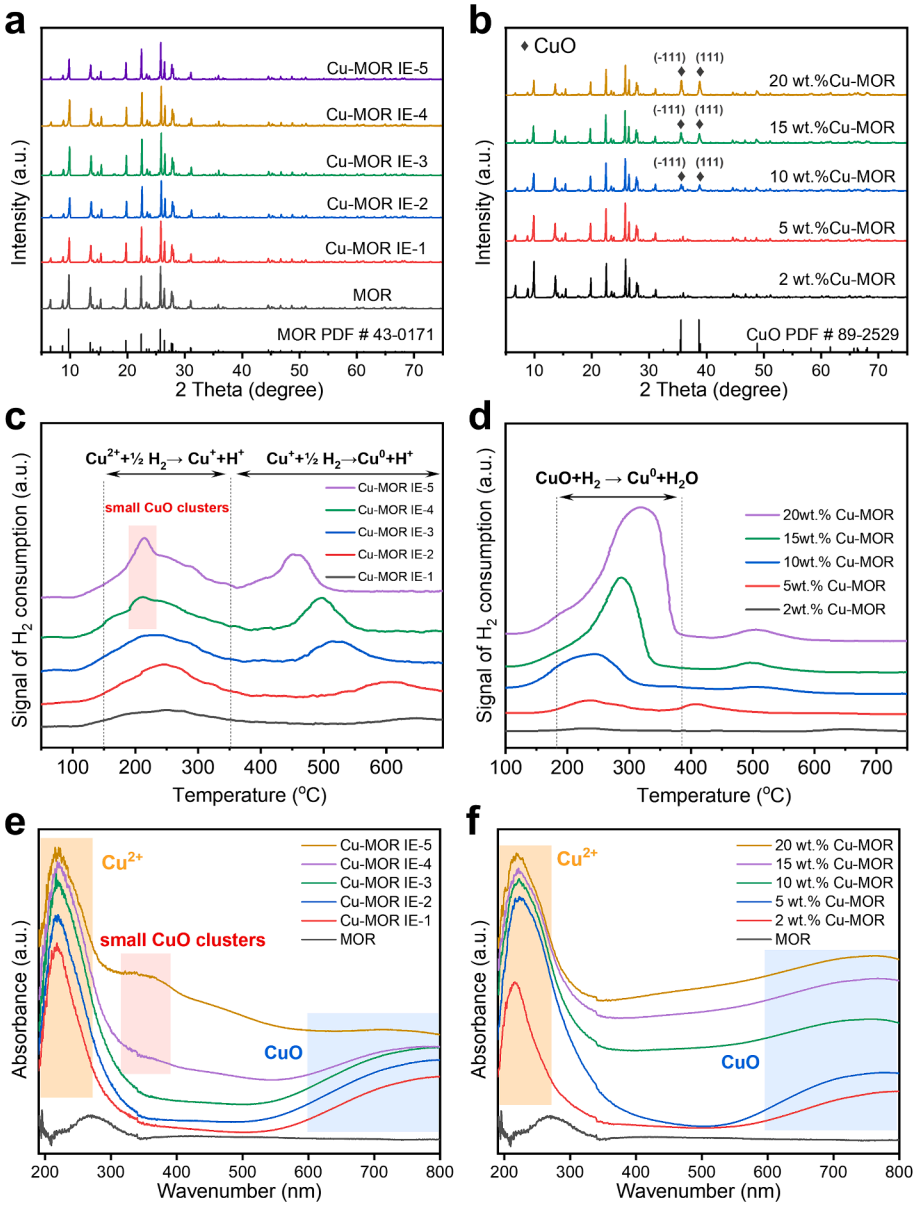

Fig. 2. Characterization of Cu-MOR catalysts prepared by ion exchange and wetness impregnation methods. (a, b) XRD patterns; (c, d) H_2-TPR profiles; (e, f) UV–Vis spectra.

of copper as CuO particles on the MOR surface, as evidenced by the XRD patterns in Fig. 2b. With increasing Cu loading, the intensity of this reduction peak strengthens and shifts toward higher temperatures, suggesting the formation of bigger CuO particles at higher loading. Additionally, a small reduction peak in the high-temperature region, corresponding to the reduction of Cu^{+} to Cu^{0}, is observed. This implies that the Cu-MOR samples prepared by wetness impregnation also contain a small amount of zeolite-confined Cu^{2+} species.

The UV–Vis spectra of the Cu-MOR samples prepared by ion exchange and wetness impregnation are presented in Fig. 2e and 2f, respectively. The absorption band at 200–300 nm is attributed to the charge transition from the MOR framework coordinated O^{2-} to zeolite-confined Cu^{2+}, including mononuclear Cu^{2+}, mono(μ-oxo) di-copper and bis(μ-oxo) di-copper species. The absorption band within the 300–500 nm range corresponds to the charge transition from coordinated O^{2-} to Cu^{2+} in small CuO clusters, including oligomeric [Cu-O-Cu] species [21]. The absorption band within the 600–800 nm range is induced by the d-d transition of Cu^{2+} within an octahedral coordination environment in the bulk CuO particles [22]. As depicted in Fig. 2e, with increasing number of ion exchanges, the peak intensities within the 200–300 nm range (corresponding to zeolite-confined Cu^{2+}) and the 600–800 nm range (corresponding to bulk CuO) both gradually increase. Notably, the peak intensities of zeolite-confined Cu^{2+} are significantly higher than those of bulk CuO, indicating a gradual increase in the content of zeolite-confined Cu^{2+}. Furthermore, the absorption band within the 300–500 nm range is clearly observed for the samples of Cu-MOR IE-4 and Cu-MOR IE-5, suggesting that an excessive number of ion exchanges leads to the presence of small CuO clusters, consistent with the H_2-TPR profiles in Fig. 2c.

The UV–Vis spectra of the Cu-MOR samples prepared through wetness impregnation with various loadings are depicted in Fig. 2f. In comparison to MOR, the Cu-MOR samples exhibit distinct absorption bands at 200–300 nm and 600–800 nm. Notably, with increasing loading, the intensities of the former peak (200–300 nm) gradually rise (2 and 5 wt% Cu-MOR) and subsequently stabilize at higher loadings (5, 10, 15 and 20 wt% Cu-MOR). This observation suggests that the

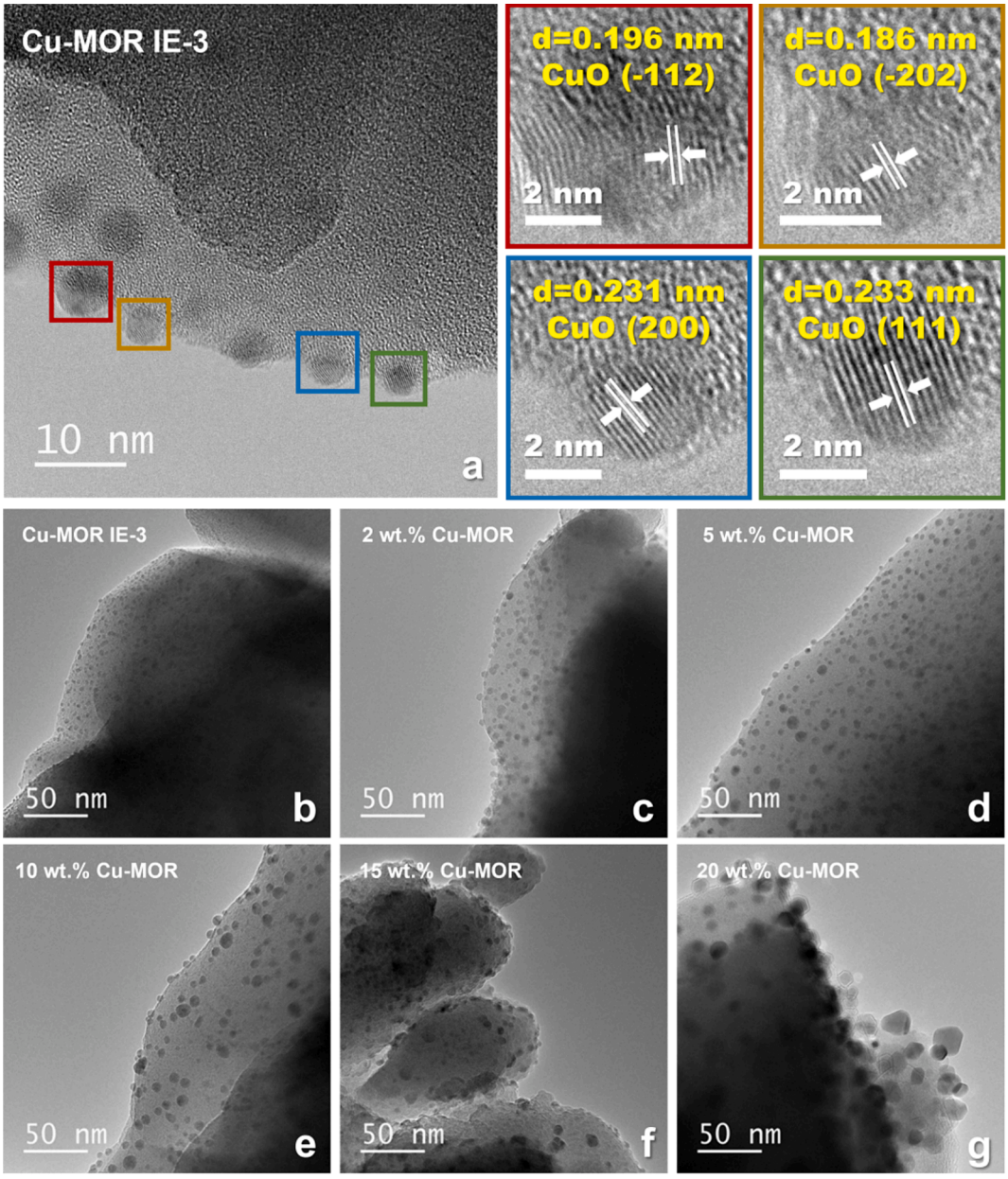

Fig. 3. HRTEM images of (a, b) Cu-MOR IE-3 (ion exchange) and (c-g) Cu-MOR prepared through wetness impregnation with various loadings.

availability of sites on MOR for anchoring zeolite-confined Cu^{2+} species is limited. Conversely, the intensities of the latter peak (600–800 nm) steadily increase with rising loading, indicating the formation of more CuO particles on MOR. This trend aligns with the XRD patterns in Fig. 2b and the H_2-TPR profiles in Fig. 2d. To distinguish the various copper species, present on the catalyst surface, we conducted CO-DRIFTS experiments. During the CO adsorption process, the intensity of the CO peak gradually increased, with the gas phase CO peak observed at 2175 cm^{-1} [23]. For the Cu-MOR IE-3 catalyst (Fig. S7a), CO adsorption occurred prominently at 2133 cm^{-1}, indicating the adsorption of CO on confined Cu^{2+} sites [24]. Conversely, in the case of the impregnated Cu/MOR catalyst (Fig. S7b), CO exhibited linear adsorption on CuO sites. This distinct shift in CO adsorption positions between the two catalysts underscores significant differences in the copper species' forms present on the catalyst surfaces.

Fig. 3 presents the HRTEM images of the Cu-MOR IE-3 sample and Cu-MOR samples with various loadings (2, 5, 10, 15 and 20 wt%). For the Cu-MOR IE-3 sample, the XRD, H_2-TPR and UV–Vis results demonstrate that most of the copper exists on MOR as zeolite-confined Cu^{2+} species, which may not be readily discerned by HRTEM. Nevertheless, some highly dispersed CuO particles are directly observed. The crystalline spacing of 0.196 nm, 0.186 nm, 0.231 nm, and 0.233 nm corresponds to the (−112), (−202), (200), and (111) crystalline planes of CuO, respectively (Fig. 3a). Although the average size of the CuO particles is approximately 3.2 nm (Fig. S8), the specific crystalline structure of our CuO particles, combined with their dispersion on the support and the potential amorphous nature of some particles, might result in the XRD signals being below the detection limit.

As depicted in Fig. 3(c-g), copper is also highly dispersed on MOR in the Cu-MOR samples prepared through wetness impregnation. However, the size of CuO particles significantly increases with increasing copper loading. The particle size distribution presented in Fig. S8 indicates that the average size of the CuO particles on Cu-MOR samples with 2, 5, 10, 15 and 20 wt% loadings is estimated to be around 4.7, 5.2, 6.8, 8.6, and 13.3 nm, respectively. Hence, it is evident that larger CuO particles are formed on Cu-MOR samples with higher loading, consistent with the findings from XRD, H_2-TPR, and UV–Vis analyses.

However, small CuO clusters, including [Cu-O-Cu] oligomers, are detected in the Cu-MOR IE-4 and Cu-MOR IE-5 samples. Our catalytic tests highlight that Cu-MOR IE-3 exhibits superior catalytic performance, while Cu-MOR IE-4 and Cu-MOR IE-5 show diminished CH_4 conversion and CH_3OH selectivity (Fig. 1a). These findings suggest that zeolite-confined Cu^{2+} species promote CH_4 conversion to CH_3OH, whereas small CuO clusters, including [Cu-O-Cu] oligomers, are less favorable for DOMtM.

The above catalyst characterization results indicate that CuO particles dominate the composition of Cu-MOR catalysts prepared through wetness impregnation. The size of CuO particles gradually increases with higher loading, even though a limited quantity of zeolite-confined Cu^{2+} is also present. Our catalytic tests (Fig. 1b) reveal that the CH_4 conversion gradually increases, but the CH_3OH selectivity decreases with rising Cu loading from 2 to 20 wt%. Additionally, the CO_2 selectivity dramatically increases with higher Cu loading. These outcomes reaffirm that CuO particles facilitate the oxidation of CH_4 to CO_2, while zeolite-confined Cu^{2+} species promote CH_3OH production. In summary, both small CuO clusters (including [Cu-O-Cu] oligomers) and bulk CuO particles are unfavorable for CH_4 conversion to CH_3OH. Therefore, we can conclude that the active sites on Cu-MOR catalysts for the selective oxidation of CH_4 to CH_3OH, driven by CH_4/O_2 plasma, are the zeolite-confined Cu^{2+} species.

To elucidate the active sites of zeolite-confined Cu^{2+} species, XPS analysis was employed to characterize the Cu-MOR catalysts prepared through ion exchange. Fig. 4a shows the Cu $2p_{3/2}$ spectra, in which we observe four peaks, corresponding to a binding energy of 944.4, 936.2,

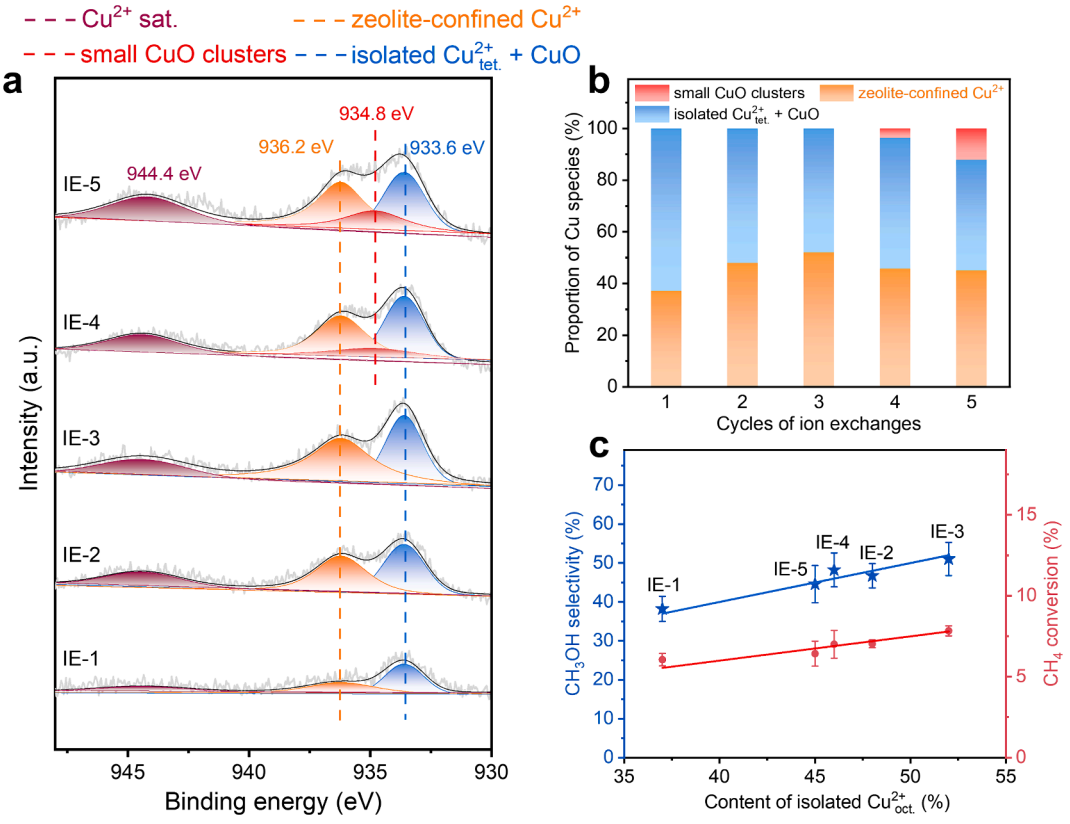

Fig. 4. XPS of the Cu-MOR catalysts. (a) Cu $2p_{3/2}$ spectra; (b) Proportion of highly dispersed Cu^{2+} and CuO species on Cu-MOR surface; (c) Relationship between highly dispersed Cu^{2+} content and reaction performance. The standard charge was calibrated by C 1 s binding energy of 284.8 eV.

934.8 and 933.6 eV. The peak at 944.4 eV is attributed to the satellite peak of Cu^{2+} species, confirming the presence of divalent Cu species (CuO and Cu^{2+}) on the Cu-MOR catalysts. Generally, the Cu $2p_{3/2}$ peaks at ca. 933.6 and 936.2 eV correspond to zeolite-confined Cu^{2+} species with tetrahedral and octahedral coordination, respectively [25]. The binding energy of CuO nanoparticles is within the range of 933.5–934.5 eV. Therefore, the peak at 933.6 eV could be assigned to both zeolite-confined Cu^{2+} species with tetrahedral coordination and CuO nanoparticles, while the peak at 936.2 eV should be attributed to zeolite-confined Cu^{2+} species with octahedral coordination, such as mono (μ-oxo) di-copper and bis(μ-oxo) di-copper species. The peak at 934.8 eV is assigned to small CuO clusters, including [Cu-O-Cu] oligomers [26].

In Fig. 4b, the relative contents of different copper species are presented for the Cu-MOR samples prepared with a different number of ion exchanges. The Cu-MOR IE-3 catalyst exhibits the highest abundance of zeolite-confined Cu^{2+} species with octahedral coordination. Conversely, Cu-MOR IE-4 and IE-5 show the presence of small CuO clusters (including [Cu-O-Cu] oligomers), consistent with the H_2-TPR results (Fig. 2c) and UV–Vis spectra (Fig. 2e). Notably, Fig. 4c illustrates a linear increase in CH_3OH selectivity and CH_4 conversion with the zeolite-confined Cu^{2+} species having octahedral coordination. Cu-MOR IE-3, with the most abundant zeolite-confined $Cu^{2+}_{oct.}$ species, exhibits the highest CH_3OH selectivity and CH_4 conversion. Conversely, Cu-MOR IE-4 and IE-5, showing the presence of small CuO clusters with decreased zeolite-confined $Cu^{2+}_{oct.}$ species, exhibit reduced CH_4 conversion and CH_3OH selectivity. These findings further underscore that zeolite-confined Cu^{2+} species with octahedral coordination, including mono (μ-oxo) di-copper and bis(μ-oxo) di-copper species, serve as the active sites for plasma-catalytic DOMtM. We conducted XPS analysis on the catalysts before and after 24 h of plasma reaction, which revealed changes in the oxidation states of Cu. Fig. S9 shows the appearance of a small amount of Cu^{+} species after the reaction, which can be attributed to the partial reduction of highly dispersed Cu^{2+} species during the reaction. Notably, the binding energies and intensities of other Cu species did not change significantly, indicating that the structure of the catalyst remained largely unchanged.

2.3. Plasma diagnosis

The Lissajous curves depicting the CH_4/O_2 plasma are presented in Fig. 5a. Notably, variations in equivalent capacitance result in distinct discharge powers when employing different packing materials. The

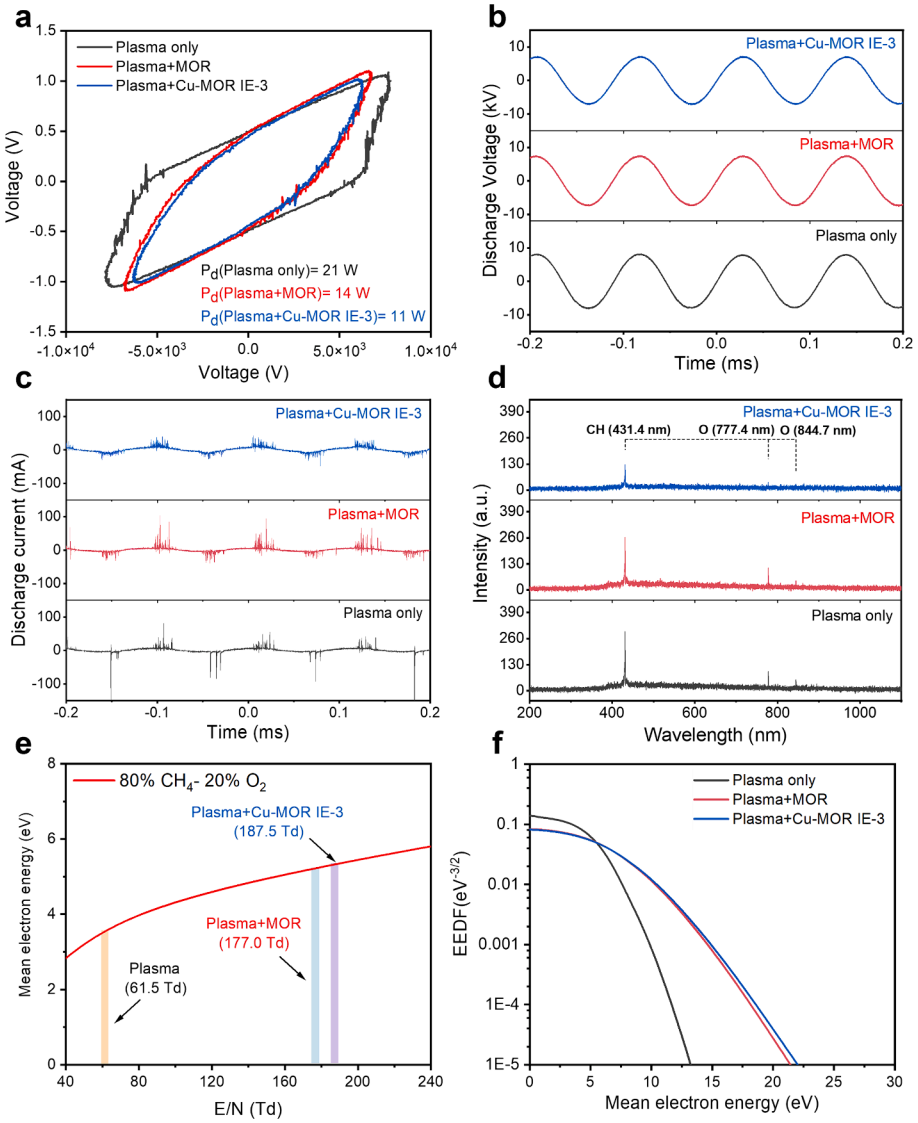

Fig. 5. Plasma diagnostics for "plasma only", "plasma + MOR" and "plasma + Cu-MOR IE-3" at the same conditions as in Fig. 1. (a) Lissajous curves; (b) Discharge voltage; (c) Discharge current; (d) *In-situ* OES results; (e) Calculated mean electron energy as a function of reduced electric field (E/N); (f) Electron energy distribution function (EEDF).

discharge power for "plasma only," "plasma + MOR", and "plasma + Cu-MOR" is 21 W, 14 W, and 11 W, respectively. The corresponding discharge voltage and current as a function of time are shown in Fig. 5b and 5c. It is evident that the packing material exhibits virtually no influence on the discharge voltage, but it does affect the discharge current, likely due to the dielectric constant of the Cu component. Indeed, the "plasma + Cu-MOR" yields lower current peaks but a higher number of pulses. Filamentary discharges facilitate the generation of reactive species, a localized electric field and surface charge accumulation at the catalyst surface and pores, thereby influencing the reactivity of the potential reactions [27,28]. The influence of current and voltage amplitudes on the catalytic performance is not significant in this work, indicating that the catalyst rather than the gas-phase is the main reaction area.

Fig. 5d shows the optical emission spectra (OES) of the CH_4/O_2 plasmas. OES lines of CH (431.4 nm, $A^2\Delta \rightarrow X^2\Pi$) and O (777.4 nm, $3s^5S^0 \rightarrow 3p^5P$ and 844.7 nm, $3s^3S^0 \rightarrow 3p^3P$) are detected, indicating the presence of a significant amount of CH and O radicals in the CH_4/O_2 plasmas [10]. Notably, the intensities of the above lines attributed to CH and O species vary with different reaction conditions. Compared with the "plasma only", the OES intensity significantly weakens after packing the CH_4/O_2 plasma with Cu-MOR catalyst. This reduction in emission intensity could be attributed to the light shielding effect of the catalyst particles, the adsorption of active species by the catalyst sites, or the energy consumption by the catalyst itself during the reaction [29–32].

The mean electron energy (MEE) and the electron energy distribution function (EEDF) for the CH_4/O_2 plasma were calculated using Bolsig+, as shown in Fig. 5e and f. The packing of catalysts significantly reduces the gas volume, leading to an evident increase in E/N. Meanwhile, the MEE in both packing systems is significantly higher than in the "plasma only" system, indicating the enhanced reactivity of the plasma species after packing (Fig. 5e). However, the MEE for MOR support and Cu/MOR catalyst are quite close, primarily determined by their differences in relative dielectric constants. Similar trends are observed in Fig. 5f, where high-energy electrons are more likely to be generated in the packing systems. We note that the variation of the discharge power dur to the catalyst packing is not a important factor for the reactivity of plasma-induced reactions. The change in discharge form and the increase in E/N could be the possible reasons for the reactivity enhancement. The discharge power is higher under "plasma only" conditions compared to "plasma + MOR" and "plasma + Cu-MOR" (Fig. 5a), which negatively correlated with the conversion results. However, the change in discharge form and the increase in E/N could be the possible reasons for the reactivity enhancement, which promote the production of high-energy species [33,33]. Consequently, the catalyst packing systems are more likely to improve the production of reactive species through electron impact dissociation, excitation, and ionization of the feedstock molecules, as well as their further reactions. The reactive species in the plasma could facilitate catalytic reactions over the MOR surface [33].

2.4. *In-situ* detection of surface species

Fig. 6 illustrates the surface species of Cu-MOR IE-3 and the 20 wt% Cu/MOR catalysts, monitored during plasma-catalytic DOMtM using *in-situ* FTIR. Following plasma activation, the peaks corresponding to surface CH_3O^* species are readily observed at 1054, 2910, and 2940 cm^{-1}, serving as key intermediates in the process of CH_3OH formation [34]. It is noteworthy that CH_3O^* is formed through combination of CH_3^* (arising from CH_4 dissociation) and O (via O_2 dissociation), consistent with the OES results in Fig. 5d. In addition, the peaks of DOMtM by-products are observed between 2400–1700 cm^{-1}, including CO_2 (2347 cm^{-1}), CO (2170 and 2115 cm^{-1}), aldehyde, and carboxylic acid products (1780 and 1750 cm^{-1}) [35,36]. In Fig. 6a, Cu/MOR IE-3 exhibits significantly higher FTIR intensity for adsorbed CH_3O^* and for CH_3OH (1015 and 1030 cm^{-1}) compared to the 20 wt% Cu/MOR

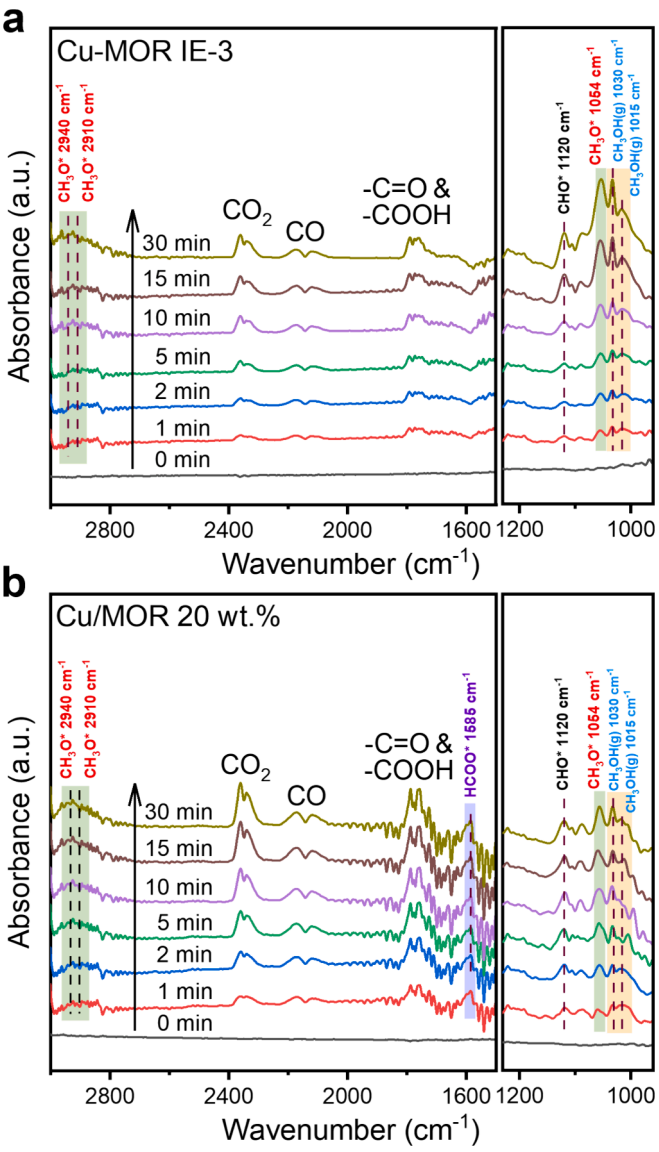

Fig. 6. *In-situ* FTIR spectra of surface species on the (a) Cu-MOR IE-3 and (b) 20 wt% Cu/MOR during plasma-catalytic DOMtM. 20 °C circulating water, discharge power 24 W, CH_4/O_2 = 4/1, flow rate = 200 mL/min.

catalyst (Fig. 6b) [37]. This emphasizes the crucial involvement of exchanged Cu^{2+} in plasma-catalytic DOMtM. Conversely, the 20 wt% Cu/MOR catalyst obtained through wetness impregnation shows higher FTIR intensity of by-products (CO_2, CO, −C=O, and –COOH). Notably, in the case of 20 wt% Cu/MOR, a new absorption band of HCOO* at 1585 cm^{-1} indicates the over-oxidation of CH_4 to CO_2 [29]. Based on the above characterizations and *in-situ* FTIR results, we can again conclude that zeolite-confined Cu^{2+} species with octahedral coordination, including mono(μ-oxo) di-copper and bis(μ-oxo) di-copper species, are the active sites for plasma-catalytic DOMtM over Cu/MOR catalysts.

3. Conclusion

We investigated the catalytic performance of Cu-MOR catalysts, prepared by ion-exchange and wetness impregnation, for plasma-catalytic DOMtM in CH_4/O_2 plasma. The Cu-MOR IE-3 catalyst, synthesized through ion-exchange, demonstrates the most favorable catalytic outcomes, with 7.9 % CH_4 conversion and 51 % CH_3OH selectivity. Conversely, the Cu-MOR catalysts prepared by wetness impregnation exhibit tendencies towards over-oxidation of CH_4 to CO and CO_2,

particularly for the catalysts with higher loadings. The combination of our catalyst characterizations reveals that ion exchange predominantly leads to the formation of zeolite-confined Cu^{2+} species within Cu-MOR, whereas wetness impregnation primarily yields CuO particles. Specifically, zeolite-confined Cu^{2+} species function as the active sites for plasma-catalytic DOMtM, while the presence of CuO clusters and particles proves detrimental to DOMtM. instead facilitating over-oxidation reactions leading to CO and CO_2 production. Finally, the surface species on the catalyst, detected by *in-situ* FTIR, further corroborate the pivotal role of zeolite-confined Cu^{2+} species in plasma-catalytic DOMtM.

CRediT authorship contribution statement

Huan Lv: Writing – review & editing, Writing – original draft, Formal analysis, Data curation, Conceptualization. **Shengyan Meng:** Writing – review & editing, Resources, Formal analysis, Data curation, Conceptualization. **Zhaolun Cui:** Writing – review & editing, Software, Formal analysis. **Shangkun Li:** Formal analysis. **Dongxing Li:** Formal analysis. **Xiaoxia Gao:** Resources, Formal analysis. **Hongchen Guo:** Resources. **Annemie Bogaerts:** Writing – review & editing, Formal analysis. **Yanhui Yi:** Writing – review & editing, Validation, Supervision, Resources, Funding acquisition, Formal analysis, Data curation, Conceptualization.

Declaration of competing interest

The authors declare that they have no known competing financial interests or personal relationships that could have appeared to influence the work reported in this paper.

Data availability

Data will be made available on request.

Acknowledgements

We acknowledge financial support from the National Natural Science Foundation of China [grant ID: 22272015], PetroChina Innovation Foundation [grant ID: 2018D-5007-0501], and Fundamental Research Funds for Central Universities [grant ID: DUT21JC40]. The research was also supported by the China Scholarship Council.

Appendix A. Supplementary data

Supplementary data to this article can be found online at https://doi.org/10.1016/j.cej.2024.154337.

References

[1] M. Ravi, V.L. Sushkevich, A.J. Knorpp, M.A. Newton, D. Palagin, A.B. Pinar, M. Ranocchiari, J.A. van Bokhoven, Misconceptions and challenges in methane-to-methanol over transition-metal-exchanged zeolites, Nat. Catal. 2 (2019) 485–494.
[2] V.L. Sushkevich, J.A. van Boichoven, Methane-to-methanol: activity descriptors in copper-exchanged zeolites for the rational design of materials, ACS Catal. 9 (2019) 6293–6304.
[3] R.A. Periana, D.J. Taube, S. Gamble, H. Taube, T. Satoh, H. Fujii, Platinum catalysts for the high-yield oxidation of methane to a methanol derivative, Science 280 (1998) 560–564.
[4] L.C. Kao, A.C. Hutson, A. Sen, Low-temperature, palladium(II)-catalyzed, solution-phase oxidation of methane to methanol derivative, J. Am. Chem. Soc. 113 (1991) 700–701.
[5] M.H. Ab Rahim, M.M. Forde, R.L. Jenkins, C. Hammond, Q. He, N. Dimitratos, J. A. Lopez-Sanchez, A.F. Carley, S.H. Taylor, D.J. Willock, D.M. Murphy, C.J. Kiely, G.J. Hutchings, Oxidation of methane to methanol with hydrogen peroxide using supported gold-palladium alloy nanoparticles, Angew. Chem. Int. Ed. 52 (2013) 1280–1284.
[6] W. Wu, W. Li, M. Wu, H. Zhang, C. Zhu, Y. Jiang, Direct oxidation of methane to methanol using $CuMoO_4$, RSC Adv. 13 (2023) 5393–5404.
[7] H.J. Kim, J. Huh, Y.W. Kwon, D. Park, Y. Yu, Y.E. Jang, B.-R. Lee, E. Jo, E.J. Lee, Y. Heo, W. Lee, J. Lee, Biological conversion of methane to methanol through genetic reassembly of native catalytic domains, Nat. Catal. 2 (2019) 342–353.
[8] M.V. Parfenov, E.V. Starokon, L.V. Pirutko, G.I. Panov, Quasicatalytic and catalytic oxidation of methane to methanol by nitrous oxide over FeZSM-5 zeolite, J. Catal. 318 (2014) 14–21.
[9] D. Li, L. Wang, X. Zhang, W. Li, Y. Ren, Z. Xie, S. Liu, L. Kong, X. Fan, X. Xiao, Z. Zhao, Effect of H_2O vapor on plasma-assisted partial oxidation of CH_4 over PtO_x/BN nanoribbon aerogel catalysts, J. Catal. 427 (2023) 115118.
[10] Y. Yi, S. Li, Z. Cui, Y. Hao, Y. Zhang, L. Wang, P. Liu, X. Tu, X. Xu, H. Guo, A. Bogaerts, Selective oxidation of CH_4 to CH_3OH through plasma catalysis: Insights from catalyst characterization and chemical kinetics modelling, Appl. Catal., B 296 (2021) 120384.
[11] H. Lv, X. Liu, Y. Hao, Y. Yi, Coupling of Dielectric Barrier Discharge and Cu-S-1 Catalyst for Direct Oxidation of Methane to Methanol, Plasma Chem. Plasma Processing 43 (2023) 1963–1978.
[12] T. Nozaki, A. Agiral, S. Yuzawa, J.G.E.H. Gardeniers, K. Okazaki, A single step methane conversion into synthetic fuels using microplasma reactor, Chem. Eng. J. 166 (2011) 288–293.
[13] A. Indarto, J.W. Choi, H. Lee, H.K. Song, Methanol synthesis over Cu and Cu-oxide-containing ZnO/Al_2O_3 using dielectric barrier discharge, IEEE Trans. Plasma Sci. 36 (2008) 516–518.
[14] P. Chawdhury, D. Ray, D. Nepak, C. Subrahmanyam, NTP-assisted partial oxidation of methane to methanol: effect of plasma parameters on glass-packed DBD, J. Phys. D-Appl. Phys. 52 (2019) 015204.
[15] Y. Tang, Y. Cui, G. Ren, K. Ma, X. Ma, C. Dai, C. Song, One-step synthesis of methanol and hydrogen from methane and water using non-thermal plasma and Cu-Mordenite catalyst, Fuel Process. Technol. 244 (2023) 107722.
[16] S. Li, R. Ahmed, Y. Yi, A. Bogaerts, Methane to Methanol through Heterogeneous Catalysis and Plasma Catalysis, Catalysts 11 (2021) 590.
[17] M. Ravi, M. Ranocchiari, J.A. van Bokhoven, The direct catalytic oxidation of methane to methanol-a critical assessment, Angew. Chem. Int. Ed. 56 (2017) 16464–16483.
[18] S.E. Bozbag, E.M.C. Alayon, J. Pechacek, M. Nachtegaal, M. Ranocchiari, J.A. van Bokhoven, Methane to methanol over copper mordenite: yield improvement through multiple cycles and different synthesis techniques, Catal. Sci. Technol. 6 (2016) 5011–5022.
[19] M. Liu, Y. Zhao, H. Zhao, X. Li, Y. Ma, X. Yong, H. Chen, Y. Li, The promotion effect of nickel and lanthanum on Cu-ZSM-5 catalyst in NO direct decomposition, Catal. Today 327 (2019) 203–209.
[20] P. Da Costa, B. Modén, G.D. Meitzner, D.K. Lee, E. Iglesia, Spectroscopic and chemical characterization of active and inactive Cu species in NO decomposition catalysts based on Cu-ZSM5, Phys. Chem. Chem. Phys. 4 (2002) 4590–4601.
[21] L. Singh, P. Rekha, S. Chand, Comparative evaluation of synthesis routes of Cu/zeolite Y catalysts for catalytic wet peroxide oxidation of quinoline in fixed-bed reactor, J. Environ. Manage. 215 (2018) 1–12.
[22] A.K.S. Clemens, A. Shishkin, P.A. Carlsson, M. Skoglundh, F.J. Martinez-Casado, Z. Matej, O. Balmes, H. Harelind, Reaction-driven Ion Exchange of Copper into Zeolite SSZ-13, ACS Catal. 5 (2015) 6209–6218.
[23] R. Ye, L. Ma, J. Mao, X. Wang, X. Hong, A. Gallo, Y. Ma, W. Luo, B. Wang, R. Zhang, M.S. Duyar, Z. Jiang, J. Liu, A Ce-CuZn catalyst with abundant Cu/Zn-O_V-Ce active sites for CO_2 hydrogenation to methanol, Nat. Commun. 15 (2024) 2159.
[24] V.L. Sushkevich, R. Verel, J.A. van Bokhoven, Pathways of Methane Transformation over Copper-Exchanged Mordenite as Revealed by In Situ NMR and IR Spectroscopy, Angew. Chem. Int. Ed. 59 (2020) 910–918.
[25] Y. Cao, L. Lan, X. Feng, Z. Yang, S. Zou, H. Xu, Z. Li, M. Gong, Y. Chen, Cerium promotion on the hydrocarbon resistance of a Cu-SAPO-34 NH_3-SCR monolith catalyst, Catal. Sci. Technol. 5 (2015) 4511–4521.
[26] L. Artiglia, V.L. Sushkevich, D. Palagin, A.J. Knorpp, K. Roy, J.A. van Bokhoven, In Situ X-ray photoelectron spectroscopy detects multiple active sites involved in the selective anaerobic oxidation of methane in copper-exchanged zeolites, ACS Catal. 9 (2019) 6728–6737.
[27] A. Sainz-Vidal, J. Balmaseda, L. Lartundo-Rojas, E. Reguera, Preparation of Cu-mordenite by ionic exchange reaction under milling: a favorable route to form the mono-(μ-oxo) dicopper active species, Micropor. Mesopor. Mat. 185 (2014) 113–120.
[28] E.C. Neyts, Plasma-Surface Interactions in Plasma Catalysis, Plasma Chem. Plasma Processing 36 (2016) 185–212.
[29] Z. Cui, C. Zhou, A. Jafarzadeh, S. Meng, Y. Yi, Y. Wang, X. Zhang, Y. Hao, L. Li, A. Bogaerts, SF_6 catalytic degradation in a γ-Al_2O_3 packed bed plasma system: A combined experimental and theoretical study, High Voltage 7 (2022) 1048–1058.
[30] S. Meng, L. Wu, M. Liu, Z. Cui, Q. Chen, S. Li, J. Yan, L. Wang, X. Wang, J. Qian, H. Guo, J. Niu, A. Bogaerts, Y. Yi, Plasma-driven CO_2 hydrogenation to CH_3OH over Fe_2O_3/γ-Al_2O_3 catalyst, AIChE J. (2023) e18154.
[31] Z. Cui, S. Meng, Y. Yi, A. Jafarzadeh, S. Li, E.C. Neyts, Y. Hao, L. Li, X. Zhang, X. Wang, A. Bogaerts, Plasma-catalytic methanol synthesis from CO_2

hydrogenation over a supported Cu cluster catalyst: insights into the reaction mechanism, ACS Catal. 12 (2022) 1326–1337.
[32] Y. Uytdenhouwen, K.M. Bal, I. Michielsen, E.C. Neyts, V. Meynen, P. Cool, A. Bogaerts, How process parameters and packing materials tune chemical equilibrium and kinetics in plasma-based CO_2 conversion, Chem. Eng. J. 372 (2019) 1253–1264.
[33] C. De Bie, J. van Dijk, A. Bogaerts, CO_2 hydrogenation in a dielectric barrier discharge plasma revealed, J. Phys. Chem. C 120 (2016) 25210–25224.
[34] Q. Chen, S. Meng, R. Liu, X. Zhai, X. Wang, L. Wang, H. Guo, Y. Yi, Plasma-catalytic CO_2 hydrogenation to methanol over CuO-MgO/Beta catalyst with high selectivity, Appl. Catal., B 342 (2024) 123422.
[35] M. Ferry, Y. Ahn, F. Le Dantec, Y. Ngono, G. Roma, Combining experimental and theoretical tools to probe radio-oxidation products in polyethylene, Polymers 15 (2023) 1537.
[36] L. Zhao, H. An, X. Zhao, Y. Wang, TiO_2-catalyzed *n*-valeraldehyde self-condensation reaction mechanism and kinetics, ACS Catal. 7 (2017) 4451–4461.
[37] Y.H. Wang, W.G. Gao, H. Wang, Y.E. Zheng, W. Na, K.Z. Li, Structure-activity relationships of Cu-ZrO_2 catalysts for CO_2 hydrogenation to methanol: interaction effects and reaction mechanism, RSC Adv. 7 (2017) 8709–8717.